


RESEARCH ARTICLE OPEN ACCESS

Detailed Bias-Dependent Free Energy Loss Analysis for Proposing Device Optimization Strategies in Silicon Heterojunction Solar Cell Design

Habtmu Tsegaye Gebrewold¹  | Karsten Bittkau² | Andreas Lambertz² | Uwe Rau^{1,2} | Kaining Ding²

¹Faculty of Electrical Engineering and Information Technology, RWTH Aachen University, Aachen, Germany | ²IMD-3 Photovoltaics, Forschungszentrum Jülich GmbH, Jülich, Germany

Correspondence: Habtmu Tsegaye Gebrewold (habtmu.tsegaye.gebrewold@rwth-aachen.de) | Kaining Ding (k.ding@fz-juelich.de)

Received: 25 April 2025 | **Revised:** 10 June 2025 | **Accepted:** 17 June 2025

Funding: HGF (Helmholtz Association)

Keywords: free energy loss | genetic algorithm | numerical simulations | silicon heterojunction solar cells

ABSTRACT

A multiscale electro-optical device model is employed to investigate free energy and other losses in a silicon heterojunction (SHJ) solar cell. A finite element method-based device model is coupled with free energy loss analysis (FELA) to calculate detailed bias voltage-dependent losses in terms of mAcm^{-2} and mWcm^{-2} . Such an approach provides insight into identifying possible pathways for synergetic optimization and redesigning a solar cell device in both laboratory and mass production settings. The SHJ solar cell investigated in this work demonstrates that the hole-selective contact (HSC) is responsible for a significant portion of the free energy loss. At maximum power point, a power density of $\sim 1.6 \text{ mWcm}^{-2}$ at 1 sun is lost associated with carrier transport in HSC and recombination at both selective contacts. This results in a 1.6% absolute loss in power conversion efficiency (PCE). Auger recombination in the wafer limits the open-circuit voltage. The FELA suggests a pathway for synergistic optimization of the device to regain a significant portion of the $\sim 2.6\%$ absolute loss in PCE. Simultaneously adjusting the conductivity of a-Si layers in HSC and the concentration of free majority carriers in the wafer can improve the fill factor (FF) to $\sim 87\%$ and PCE close to 26%.

1 | Introduction

The solar spectrum arriving at the earth's surface varies mainly due to atmospheric effects, local conditions, latitude, and seasons. The green-shaded curve in Figure 1 shows the global standard solar spectrum (AM1.5g) at the earth's surface [1]. It represents the solar irradiance at the earth's surface, including direct and diffuse radiation. The AM1.5g spectrum is used as a standard reference spectrum for comparing the performance of solar cells. The blue-shaded region in Figure 1 represents the actual absorption spectrum of a 24.5% efficient front- and back-contact (FBC) silicon heterojunction (SHJ) solar cell from our institute [2]. This back junction (BJ) solar cell is certified by the Institute for Solar Energy Research in Hamelin (ISFH). It is used for the study in this work.

Integrating the spectral irradiances of the shaded curves in Figure 1, a total power density of $\sim 1.3 \times 10^3 \text{ Wm}^{-2}$ is calculated for AM0 and $\sim 1.0 \times 10^3 \text{ Wm}^{-2}$ for AM1.5g. Assuming a unity quantum yield, for each spectral photon, the maximum theoretical photocurrents are $J_{\text{ph, AM0}} \approx 98.45 \text{ mAcm}^{-2}$ for AM0 and $J_{\text{ph, AM1.5g}} \approx 68.75 \text{ mAcm}^{-2}$ for AM1.5g. Hence, calculating the total photon flux of the standard AM1.5g spectral irradiance arriving at the earth's surface, the overall spectrum yields a potential total current density of 68.75 mAcm^{-2} . The wavelength range of 280 nm to 1200 nm is the active absorption range of silicon, the active absorber material in conventional solar cells. The total potential photocurrent density in this spectral range is $\sim 46.3 \text{ mAcm}^{-2}$. Adequately designed solar cell devices are reported to produce a short-circuit current density above 86%

This is an open access article under the terms of the [Creative Commons Attribution](https://creativecommons.org/licenses/by/4.0/) License, which permits use, distribution and reproduction in any medium, provided the original work is properly cited.

© 2025 The Author(s). *Solar RRL* published by Wiley-VCH GmbH.

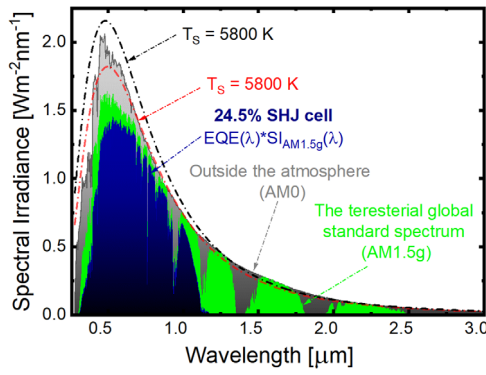


FIGURE 1 | The shaded areas represent the actual spectral irradiance outside the atmosphere AM0 (black) [1], the terrestrial global standard spectrum AM1.5g (green) [1], and the spectrum absorbed by our ISFH-certified SHJ cell with a 24.5% efficiency [2] (presented in Sections 3 and 4). The broken lines represent black body irradiance in $\text{Wm}^{-2}\text{nm}^{-1}$ outside the earth's atmosphere, calculated according to Kirchhoff's law of radiation for different black body temperature assumptions of the sun [3].

for silicon single junction silicon solar cells [4, 5] and above 90% for silicon-based tandem solar cells of the 46.3 mAcm^{-2} limit [6, 7]. However, these theoretical electric current density limits are impossible to reach due to the inevitable losses with any practical device, yet it can be further designed to fine-tune it to get closer. Furthermore, transporting charge carriers introduces other parasitic energy losses in an actual device. In this work, we used a multiscale model of SHJ solar cells, incorporating detailed materials parameters and physical models, to estimate realistic device optical and electrical responses. The model is validated using measurements of our ISFH-certified solar cell. We implemented the FELA at every node point of the virtual device representation mesh of the Sentaurus Technology computer-aided design (TCAD) device model of the SHJ solar cell. We showed that such a model, coupled with FELA, provides detailed current and power density loss mechanisms. It enables us to identify which layers and which loss mechanism contribute significantly. We limited the scope of this manuscript. It presents optimization strategies excluding a significant effect on the device's optical response. The model can also be expanded for SHJ-based tandem solar cells. This work provides a basic understanding of pathways and recommends an approach to designing efficient SHJ solar cells by utilizing detailed bias-dependent current and power density loss analysis.

2 | Free Energy Loss Analysis in SHJ

Photogenerated electron-hole pairs in a single bandgap absorber material lose the energy of the absorbed photons due to thermalization and entropy-related losses. Therefore, only the available free energy can be extracted as electrical energy at the terminal, even in an ideal, lossless conventional device design. In practice, however, the charge carriers must be dissociated, separated, and transported to the corresponding electrodes that connect to the load. The process of transporting will encounter carrier transport loss as joule heat. Furthermore, the carriers will face different material properties, such as recombination centers, at the bulk and interface

regions. One can use the so-called FELA to quantify these losses. FELA is a technique derived and introduced by Brendel et al. [8, 9]. It helps to express losses associated with fundamental processes in terms of energy rate per cell area in units of mWcm^{-2} . The energy rate losses due to carrier recombination and transport are expressed in mWcm^{-2} and can be directly compared to the total input power density of the AM1.5g spectrum. In the scope of this work, the total input power density integrated over the wavelengths of the AM1.5g spectrum is 100 mWcm^{-2} .

Here, FELA is implemented on the electro-optical model of the solar cells. The relevant quantities are directly calculated at each positional mesh point in the 2D virtual representation of the solar cell device. These quantities are presented as follows. The theoretical maximum power density remaining in an ideal device after thermalization and optical losses can be calculated as the integration of the product of the optical generation rate with the local bandgap (E_G) of the materials in the device,

$$P_{E_G} = \frac{1}{A_{\text{cell}}} \int G(r) * (E_C(r) - E_V(r)) dV \quad (1)$$

where P_{E_G} represents the optically limited ideal power density in an ideal device after accounting for optical and thermalization losses. $G(r)$ is the photogeneration rate in $\text{cm}^{-3}\text{s}^{-1}$, at a position r in the device, and A_{cell} is solar cell area or the electro-optically modeled area of the device. $E_C(r)$ and $E_V(r)$ are the bottom and upper edge energy levels of the conduction and valence bands, respectively, at a position r . The ideal free power density output of a solar cell device (P_{eh}) can be calculated as the integration of the product of the optical generation rate and the associated local electrochemical potential energy of the electron-hole pairs or the quasi-Fermi level splitting (ΔE_F), i.e.,

$$P_{\text{eh}} = \frac{1}{A_{\text{cell}}} \int G(r) * E_{\text{eh}}(r) dV = \frac{1}{A_{\text{cell}}} \int G(r) * (E_{\text{Fn}}(r) - E_{\text{Fp}}(r)) dV \quad (2)$$

where E_{eh} is the electrochemical potential energy, in eV, of the generated electron-hole pairs ($E_{\text{eh}} = \Delta E_F = E_{\text{Fn}} - E_{\text{Fp}}$). However, the free energy can't be fully extracted in real devices. There are losses associated with fundamental processes in real devices. The losses include the recombination of generated electron-hole pairs in the bulk and at the surfaces, as well as power loss due to carrier transport. The recombination losses in the bulk regions are quantified in terms of power density loss as follows

$$P_R = \frac{1}{A_{\text{cell}}} \int R(r) * E_{\text{eh}}(r) dV = \frac{1}{A_{\text{cell}}} \int R(r) * (E_{\text{Fn}}(r) - E_{\text{Fp}}(r)) dV \quad (3)$$

where $R(r)$ is the recombination rate, in $\text{cm}^{-3}\text{s}^{-1}$, of the photogenerated electron-hole pairs at a position r in the device and P_R is the power density loss due to recombination rate $R(r)$. The bulk recombination processes include Shockley-Read-Hall (SRH), radiative, and Auger recombination. Hence, the power density loss P_R^{Rad} , P_R^{Aug} , P_R^{SRH} or P_R^{Total} are calculated by replacing the recombination rate $R(r)$ with $R_{\text{Rad}}(r)$, $R_{\text{Aug}}(r)$, $R_{\text{SRH}}(r)$, and $R_{\text{Tot}}(r)$, respectively, for individual recombination processes and

their total. Surface recombination losses can be represented by a surface recombination current density. Considering the surface as a sinking plane for the electron-hole pairs, it can be assumed by the minimum of the electron or hole current density of the sinking carriers via surface

$$P_R^{\text{Surf}} = J_{\text{surf}}^{\text{min}} * \frac{E_{\text{eh}}(r_s)}{q} = J_{\text{surf}}^{\text{min}} * \frac{E_{\text{Fn}}(r_s) - E_{\text{Fp}}(r_s)}{q} \quad (4)$$

where q is the elementary charge, r_s indicates the position of the surface, P_R^{Surf} power density loss at the surface via surface recombination, and $J_{\text{surf}}^{\text{min}}$ is the current density of the minority carrier at that specific contact side. Electrons are minority carriers at the HSC, and holes are minority carriers at the ESC of a solar cell.

The carrier transport-related power density loss for carriers driven by the electrochemical gradient can be quantified for either carrier type as an integration of the square of local carrier current density divided by the corresponding carrier type conductivity

$$P_t^{\text{e,h}} = \frac{1}{A_{\text{cell}}} \int \frac{|J_{\text{e,h}}(r)|^2}{\sigma_{\text{e,h}}(r)} dV \quad (5)$$

where P_t^{e} or P_t^{h} are power density loss related to electron or hole transport, respectively. $J_{\text{e}}(r)$ or $J_{\text{h}}(r)$ are the electron or hole, respectively, current density at a position r . $\sigma_{\text{e}}(r) = qn(r)\mu_{\text{e}}(r)$ and $\sigma_{\text{h}}(r) = qp(r)\mu_{\text{h}}(r)$ are the electron and hole conductivities, respectively, at a position r . $\mu_{\text{e}}(r)$ and $\mu_{\text{h}}(r)$ are electron and hole mobilities, respectively.

3 | Electro-Optical Model of SHJ Solar Cell

The schematic depiction of a typical SHJ solar cell, as used in this work, is shown in Figure 2. A multiscale device model of SHJ cells is developed using Sentaurus TCAD. A similar approach was used in our previous work [10]. Here, the physical device equations governing the operation of a solar cell, a set of differential equations, are numerically solved for a finite-element mesh-based virtual representation of the physical device. The optical response of the solar cell is simulated using ray tracing in the thick crystalline silicon layer, coupled with the transfer

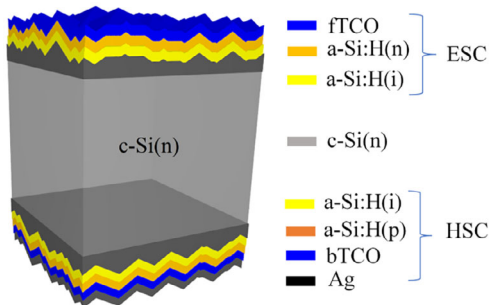


FIGURE 2 | A 3D schematic depiction of a SHJ solar cell of n-type c-Si absorber layer with electron selective contact (ESC) and hole selective contact (HSC) as layer stacks of hydrogenated amorphous silicon (a-Si:H) and transparent conductive oxide (TCO).

matrix method for the contact thin films. For these, the optical properties of most materials are obtained from spectroscopic ellipsometer measurements, while some are taken from the literature [11, 12]. Afterward, the resulting optical generation profile from the optical simulation is used for a subsequent electrical simulation. The generation profile is adapted from the 3D optical simulation to be used in the 2D simulation window, with a half-pitch size of the front metalization contact of the mono-facial solar cell. The finger pitch represents the separation distance between consecutive fingers. The physics of charge-carrier dynamics, including dissociation and collection of the generated electron-hole pairs, is modeled based on the so-called drift-diffusion model. Furthermore, the carrier dynamics in the defective a-Si:H layers are implemented as in SentaurusTCAD [13]. The FELA equations, Equations (1) – (5), are implemented directly at each node in the virtual representation mesh of the physical device.

The device model approach described above is employed to model the SHJ solar cell, which has an ISFH-certified efficiency of 24.5% [2]. The basic input parameters and specific property models used for the SHJ solar cell electro-optical device model are given in Table 1. A 3D optical simulation is performed within a $10 \mu\text{m} \times 10 \mu\text{m}$ simulation window, featuring a randomized front and back textured surface with a perfect reflection boundary condition. The external quantum efficiency ($\text{EQE}(\lambda)$) is calculated from the contribution of the modeled absorption in the crystalline silicon and 30% of the absorption in the a-Si (i) layer. Furthermore, a 3.5% shading loss is accounted for due to the shading effect of the front metalization. At the rear side, full metalization is assumed. We employed a genetic algorithm-based optical fitting of the measured $\text{EQE}(\lambda)$ for the ESC layers [10]. The fitting thicknesses found are 100 nm of magnesium fluoride (MgF_2) antireflection coating (ARC) on top of the layers' thicknesses given in Table 1. The calculated $\text{EQE}(\lambda)$ closely matches the measured $\text{EQE}(\lambda)$, as shown in Figure 3b. The estimated short-circuit current density (J_{SC}) agrees with the measured value of $\sim 39.5 \text{ mAcm}^{-2}$. Note that a 70 nm MgF_2 layer is considered at the rear side, between the indium tin oxide (ITO) and silver (Ag) [2]. The MgF_2 layers at the front and rear sides are assumed to have only an optical impact and are considered only in the optical model of the solar cell. Trap state distributions in the hydrogenated a-Si:H layers and interfaces used in this work, as shown in Table 1, are adapted from the literature. The front and rear side a-Si:H (i) layers, as well as the c-Si/a-Si:H (i) interfaces, are assumed to have identical properties for brevity. In this assumption, the identical properties on both sides represent the average effect of the experimentally nonidentical properties of the two sides. The active dopant concentrations of the doped layers are given in Table 1. A spatially uniform doping and trap state distribution profiles are considered for the respective layers and materials. A $1.0 \text{ m}\Omega\text{cm}^{-2}$ contact resistivity is used for both front and back ITO/Ag metal contacts. On the sides, ideal Neumann boundary condition is considered as the default noncontact boundary condition in Sentaurus TCAD [13]. The device model assumes a perfectly conductive metal. The model is validated to agree with the measured current density versus bias voltage $J(V)$ result, as shown in Figure 3b. The slight deviation between the simulation and measurement around the bias voltage of 700 mV may relate

TABLE 1 | Summary of basic input, a-Si:H materials trap states, and interface parameters used for simulations of the SHJ solar cell in this work [2].

Optical input				
Solar spectrum	AM1.5g			
Generation profile	3D optical simulation of the device using Sentaurus TCAD			
Front metal contact				
Pitch	1600 μm			
Finger width	40 μm			
c-Si				
Free carrier statistics	Fermi–Dirac			
Temperature	300 K			
Auger and radiative recombination	Richter et al. [14], Nguyen et al. [15]			
Intrinsic carrier density	Altermatt et al. [16] (9.65 × 10 ⁹ cm ^{−3} at T = 300 K)			
Wafer resistivity	1.0 Ωcm, n-type/ N _D = 4.945 × 10 ¹⁵ cm ^{−3}			
Mobility	Klaassen [17]			
Bulk SRH lifetime	20 ms			
Thickness	135 μm			
SHJ side contact	a-Si:H (n)	front back a-Si:H (i)	a-Si:H (p)	front back ITO
Thickness [nm]	1.7	4.3 6	13	62
Band gap [eV] ^a	1.7	1.7	1.7	3.7
Electron affinity [eV] ^a	3.9	3.9	3.9	4.9
Dielectric constant ^a	11.7	11.7	11.7	4.7
Electron/hole mobility [cm ² V ^{−1} s ^{−1}]	0.75/0.15	0.6/0.12	0.75/0.15	28
Barrier tunneling mass (Electron/hole) [m/m ₀] ^b	—	0.1/0.1 [18]	0.1/0.1 [18]	0.1/0.1 [18]
Active dopant conc. [cm ^{−3}]	2.0 × 10 ²⁰	–	9.5 × 10 ¹⁹	1.5 × 10 ²⁰
Effective DOS (N _C /N _V) [cm ^{−3}] ^a	(2.0/2.0) × 10 ²⁰	(2.0/2.0) × 10 ²⁰	(2.0/2.0) × 10 ²⁰	(0.4/1.7) × 10 ¹⁹
Materials defects ^c	a-Si:H (n)	a-Si:H (i)	a-Si:H (p)	
Urbach energy (VB/CB tails) (eV)	0.094/0.068	0.05/0.035	0.12/0.08	
Urbach tail pre-factor (cm ^{−3} eV ^{−1})	2 × 10 ²¹	1.88 × 10 ²¹	2 × 10 ²¹	
Urbach tail e/h capture cross section (cm ²)	7 × 10 ^{−16} /7 × 10 ^{−16}	7 × 10 ^{−16} /7 × 10 ^{−16}	7 × 10 ^{−16} /7 × 10 ^{−16}	
Gaussian peak defect density (cm ^{−3} eV ^{−1})	1.31 × 10 ²⁰	1.38 × 10 ¹⁶	1.31 × 10 ²⁰	
Gaussian donor/acceptor standard deviation (eV)	0.21	0.21	0.21	
Gaussian donor/acceptor peak position from VB (eV)	0.5/0.6	0.89/1.09	1.1/1.2	
Gaussian donor e/h capture cross section (cm ²)	3 × 10 ^{−14} /3 × 10 ^{−15}	3 × 10 ^{−14} /3 × 10 ^{−15}	3 × 10 ^{−14} /3 × 10 ^{−15}	
Gaussian acceptor e/h capture cross section (cm ²)	3 × 10 ^{−15} /3 × 10 ^{−14}	3 × 10 ^{−15} /3 × 10 ^{−14}	3 × 10 ^{−15} /3 × 10 ^{−14}	
Interface defects ^d	a-Si:H (i)/ c-Si (n)			
Uniform interface defect density (cm ^{−2} eV ^{−1})	3 × 10 ⁹			
Donor defect states energetic distribution from VB (eV)	[0.06–0.56]			
Acceptor defect states energetic distribution from VB (eV)	[0.56–1.06]			
Donor capture cross section (e/h) (cm ²)	10 ^{−14} /10 ^{−14}			
Acceptor capture cross section (e/h) (cm ²)	10 ^{−14} /10 ^{−14}			

^a[19].^b m_0 is electron rest mass.^cAdapted from [19–23].^dAdapted from [21].

to the parametrization of Auger recombination [14, 24, 25]. It is the dominant recombination mechanism for the bias voltage range above the maximum power point (MPP) of 645 mV,

discussed in Sections 3 and 4. The conventional solar cell performance parameters from the TCAD model simulation (measurement) are J_{SC} of 39.5 mAcm^{-2} (39.5 mAcm^{-2}), open-circuit

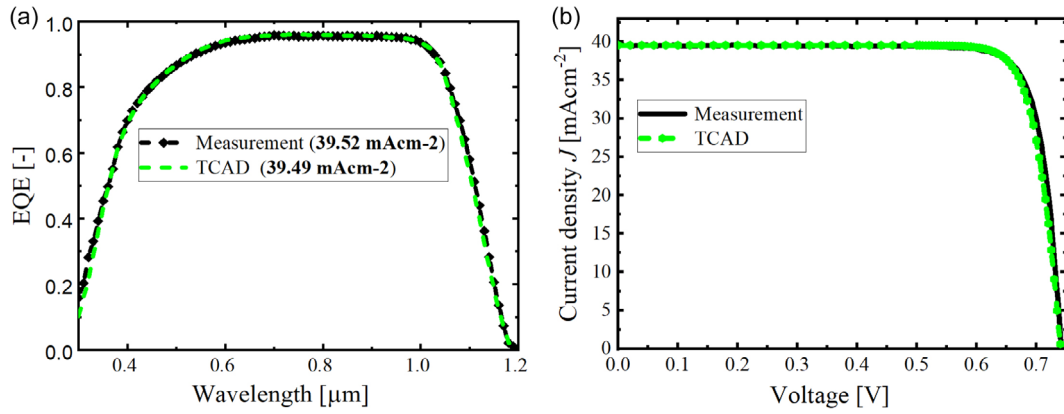


FIGURE 3 | Comparison of experimental measurement [2] and TCAD model (a) $EQE(\lambda)$ and (b) current density versus bias voltage $J(V)$ of FBC-SHJ solar cell. A 3.5% shading loss is accounted for the shading effect of front metalization. A summary of the main input parameters used for the TCAD model is given in Table 1. Additionally, the ISFH-certified SHJ solar cell features a ~ 100 nm MgF_2 antireflection coating (ARC) and a 70 nm MgF_2 layer positioned between ITO and Ag back reflector on the rear side [2].

voltage (V_{OC}) of 741 mV (742 mV), FF of 83.7% (83.6%), and PCE of 24.5% (24.5%).

The losses that hamper the solar cell device's efficiency are diverse and multi-type. These include optical losses, recombination losses due to defects or otherwise, carrier transport-related losses, and other fundamental losses. The fundamental thermodynamic losses are thermalization loss and entropy generation [26]. In the following, we attempt to present most of these losses in order, starting from optical losses, in terms of current density and power density within the scope of this work.

4 | Current Density Losses

An efficient solar cell absorbs most of the incident photon flux of the standard AM1.5g spectral irradiance to generate electron-hole pairs in its active layer. The remaining photon flux is lost through reflection or parasitic absorption. The absorption in layers that may generate short-lived electron-hole pairs can't be separated and collected. These losses are called optical losses. We consider optical losses to be independent of the solar cell's bias voltage. The bias voltage determines the relationship between the extracted output current density and the carrier concentration in the active layer. A high carrier concentration in the active material results in a high rate of carrier loss due to both bulk and surface recombination. A detailed dependence of the different recombination mechanisms on carrier concentration can be found elsewhere [3, 14–16, 25, 27, 28]. The models and parameters used in this work are given in Table 1. The optical and recombination losses are detailed below.

4.1 | Optical Losses

The optical losses are presented in Figure 4 for the modeled ISFH-certified SHJ cell, which features an Ag back reflector, a 100 nm MgF_2 antireflection coating, and a 70 nm MgF_2 interlayer between ITO and Ag, as reported by Duan et al. [2]. One can see that, within the wavelength range of 0.3–1.2 μm , the most significant optical loss of 3.59 mAcm⁻² is due to reflection. Secondly, the front and rear side ITO absorb almost 1.7 mAcm⁻² in total. We also lose

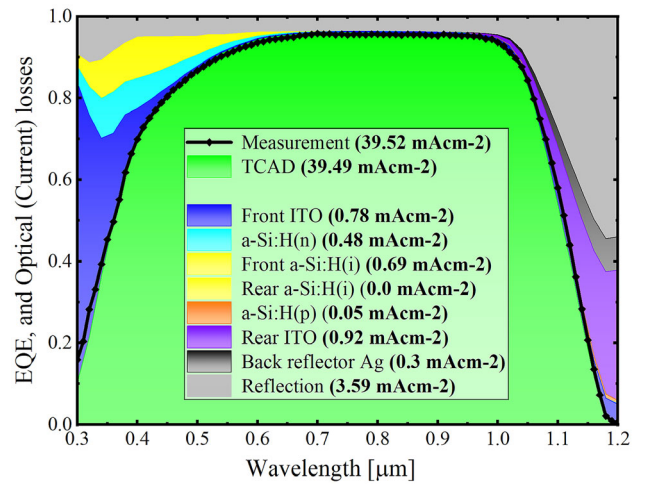


FIGURE 4 | EQE measurement vs. simulation and current losses of SHJ cell. 3.5% shading loss accounts for the shading effect of front metalization, and 30% of photons absorbed on the front side a-Si:H (i) is assumed to contribute to the EQE of the cell.

via parasitic absorption in the doped a-Si:H layer and from partial absorption loss in the intrinsic a-Si:H layers. Almost all the current loss in a-Si layers comes from the front side layers rather than the rear side. It is because a significant portion of the light intensity for most of the spectrum, up to the near-infrared regime, is absorbed either at the front contact layers or within a few micrometers of the active layer (c-Si (n)). The a-Si:H layers exhibit insignificant absorption in the near-IR and IR regions of the spectrum. Instead, the rear-side ITO and Ag back reflector absorb some portion of the photon flux corresponding to these longer-wavelength spectra. The remaining intensity will either be absorbed mainly within the wafer through multiple back-and-forth light travels or be lost as reflection through the front contact.

4.2 | Recombination Losses

For c-Si-based solar cells, absorption of light with wavelengths above 1.2 μm is negligible. Hence, assuming a unity quantum

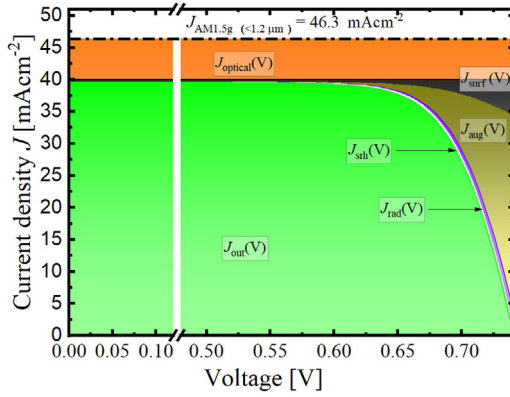


FIGURE 5 | Current density vs. voltage for the SHJ solar cell and equivalent current densities for different types of current loss.

yield and a spectral power density according to AM1.5g, the total possible photocurrent density available is 46.3 mAcm^{-2} . This would only be achieved if all incident photons are absorbed, creating a corresponding electron–hole pair. As discussed above, more than 6 mAcm^{-2} of the incoming light is lost due to reflection or parasitic absorption. These optical losses are not significantly dependent on the bias voltage; therefore, assuming them to be constant during $J(V)$ measurements or simulations is justified. With this assumption, we could model detailed losses by decoupling the optical and electrical aspects of the electro-optical device. However, the current losses due to recombination depend on the bias voltage, as discussed above. In Figure 5, current losses are given as a function of the bias voltage. At a short-circuit condition, the output current density is almost identical to the expected photocurrent after the optical losses, except for a small amount of surface recombination loss. However, as the bias voltage increases, the carrier density, especially for the minority charge carriers, increases, resulting in a larger quasi-Fermi level splitting and higher recombination loss rate. At an open-circuit condition, all the photocurrent generated from absorption in the active layers will be lost due to recombination. The dominant recombination type is Auger recombination; hence, the open-circuit voltage of the SHJ solar cell modeled here is limited by Auger recombination.

5 | Electro-Optical Detailed Free Energy Losses of SHJ Solar Cell

As discussed in Section 2, FELA is a technique that helps to express losses associated with fundamental processes of device operation in terms of energy rate per cell area in units of mWcm^{-2} [9–30, 26, 29–31]. In this work, the total input power density integrated over the wavelength of the AM1.5g spectrum is calculated to be 100 mWcm^{-2} . The bias voltage-dependent free energy losses, calculated from a Sentaurus TCAD electro-optical model simulation of our SHJ solar cell, are shown in Figure 6.

As shown in Figure 6, the primary free energy loss for bias voltages below $\sim 630 \text{ mV}$ is attributed to hole (minority charge carrier) transport to the rear-side contact. Most of the optical absorption occurs within a few micrometers of the wafer's surface. Hence, the resulting electron–hole pairs are generated near

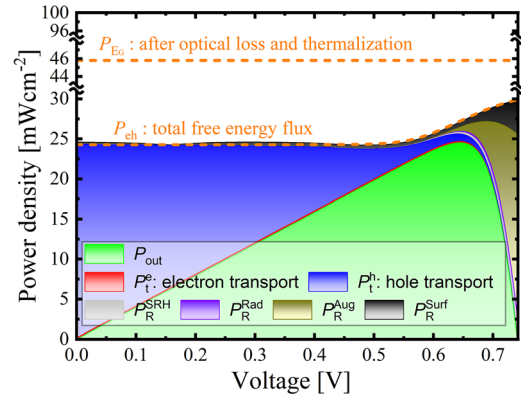


FIGURE 6 | FELA at different bias voltages for the SHJ solar cell. The free energy rate losses versus bias voltage are calculated using the device model of the SHJ solar cell, as presented in Figure 3. P_e^e and P_h^h stand for power density losses related to electron and hole transport, respectively, including at ITO/Metal contacts. P_R^{Rad} , P_R^{Aug} , P_R^{SRH} , and P_R^{Surf} stand for power density loss due to radiative, Auger, SRH, and total surface recombination, respectively. The broken orange lines represent the theoretical power densities. P_{eh} is power density corresponding to the free electrochemical potential energy of the electron–hole pairs. P_{Eg} is power density of theoretically available energy after thermal relaxation and optical losses. The difference between the two orange lines shows other (entropy related) losses.

the wafer's front surface. The holes will have to travel through the wafer accompanied by ohmic loss in the wafer. Afterward, the holes face the valence band offset at the c-Si/a-Si:H (i) interface and must travel toward the a-Si:H (p)/ITO interface. The transport involves both conventional valence band transport in thin layers of a-Si:H (i, p) and transport via trap-assisted and band-to-band tunneling. Through band-to-band tunneling, the holes recombine at the a-Si:H (p)/ITO interface with an equal number of electrons from the TCO/Ag contact. These processes of hole transport and collection are performed by paying off part of the free energy as a loss. The total hole transport-related free energy current loss is shown in the blue area in Figure 6, while in Figure 7b, the total energy current loss is decomposed to the hole transport-related energy loss at each layer. For a low bias voltage, the hole transport-related free energy loss in the wafer makes the dominant contribution, followed by the loss in the intrinsic a-Si:H layer on the rear side. For bias voltages above 600 mV , however, the hole transport-related energy loss in the wafer decreases and becomes almost insignificant, as shown in Figure 7b.

The hole transport-related energy loss at the rear side intrinsic a-Si:H is dominant at higher voltage. The free energy loss related to electron transport has a minimal contribution compared to hole transport. Here, it is apparent that the main carrier transport-related free energy loss comes from the wafer in low bias voltage region and significant contribution from the rear side a-Si:H layers near V_{OC} , see Figure 7a. In fact, near a short-circuit condition, the free energy loss is primarily a minority carrier transport-related power density loss in the wafer. At 0.0 V bias, we can visualize holes moving down, with respect to the hole energy axis, along the electrochemical energy gradient before recombining with electrons from the opposite contact at the same energy level. The recombination of the extracted electrons and

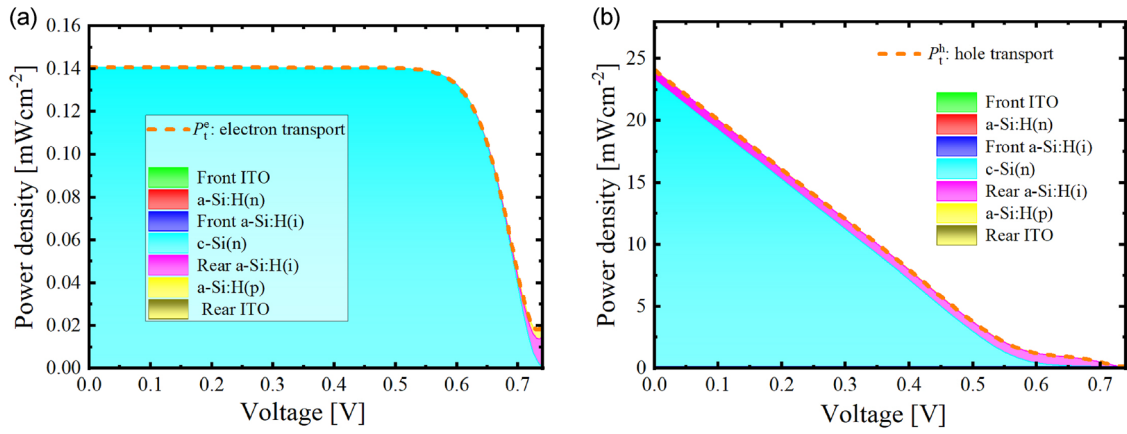


FIGURE 7 | Carrier, (a) electrons, and (b) holes, transport-related power density loss in mWcm^{-2} ; Sentaurus TCAD device simulation of SHJ solar cell discussed above. P_t^e and P_t^h stand for the power density losses related to electron and hole transport in the device, respectively.

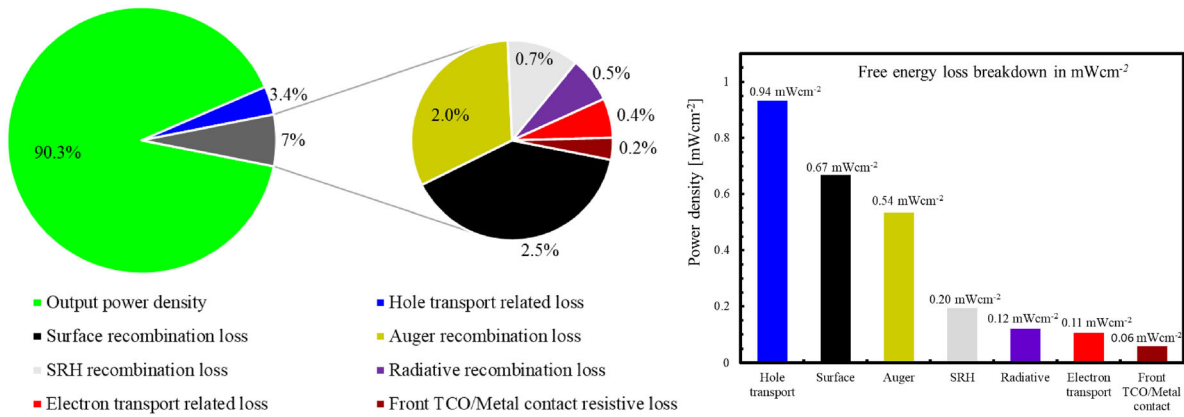


FIGURE 8 | Detailed free energy breakdown of the dominant processes in the SHJ solar cell at MPP.

holes at the external circuit has no potential electrochemical energy left for conversion to perform output work. At MPP, the power density loss at the rear a-Si:H significantly degrades the solar cell's performance. Hole transport-related power density loss amounts to $\sim 3.4\%$ of the total power density corresponding to the available free energy at the MPP. It also corresponds to a FF loss of $\sim 3.8\%$ of the current FF, which is an absolute loss of $\sim 3.2\%$ in FF. There is approximately a 3.6% absolute loss in FF if we include electron transport-related losses. This value puts in an ideal scenario FF beyond 87% . The detailed power density losses and power output at a bias voltage corresponding to the MPP are presented in Figure 8 as a pie chart and a bar chart. Insignificant loss mechanisms are ignored in the charts. A resistive loss of $1.5 \mu\text{Wcm}^{-2}$ (0.06% of the total loss) is calculated for rear side TCO/Ag contact. Note that full metalization is assumed on the rear side.

In Figure 6, two broken orange lines are added, as defined in Section 2. The top one does not exclude the entropy-related loss. This line has a voltage bias independent value of around 45.8 mWcm^{-2} . It is the value of the theoretical, potentially available, remaining energy of the photogenerated electrons in the conduction band and holes in the valence band after thermal relaxation for absorbed photon energies above the bandgap, as shown in Equation (1). However, a significant amount of power

density is lost by entropy creation [9, 26, 32, 33]. The second orange line is the available free electrochemical potential energy density per second. As one can see, this value is below 30 mWcm^{-2} for our cell and will reach around 30 mWcm^{-2} at V_{OC} . Here, it can be explained by a lower entropy creation near V_{OC} as compared to the case of low bias voltage with low concentration of free carriers in the device. Brendel et al. and others explain this relation by stating that a high carrier concentration corresponds to a small entropy per charge carrier particle [9, 34]. Hence, entropy will increase when the device's steady-state free carrier concentration decreases via extraction or recombination. From our device performance perspective, however, it has little consequence since all the free energy is lost at V_{OC} within the device, as shown in Figure 6. Nonetheless, it suggests that MPP must be shifted toward V_{OC} which is the idea captured by the FF as a conventional solar cell performance parameter. Note that near short-circuit conditions, as shown in Figure 6 and other similar plots, the summation of the individual losses may overestimate the power density of available free electrochemical potential energy rate density. We attribute the deviation to numerical inaccuracy due to the high current density and small, non-uniform quasi-Fermi level splitting in the implemented equation of the device model with a finite mesh size. This could be true, particularly for transport-related loss calculations in Equation (5), which includes a squared current density term.

6 | Strategy and Pathways for Device Optimization

Every aspect of the electro-optical mechanisms of solar cell devices is coupled. Optimization of a single aspect of the device can have an adverse effect on other aspects of the solar cell device. For example, improving surface recombination can increase carrier concentrations at MPP in the active layer, thereby affecting other carrier-dependent processes. It will increase the free energy, or Fermi-level splitting, and bulk recombination, as shown in Figure 9. Hence, the net effect of improving the wafer surface is a tradeoff between the consequences of these coupled effects. Figure 9 shows the impact of a-Si (i)/c-Si (n) interface defect density on the solar cell power density output and detailed power density losses at the MPP. Similar to the discussion in the previous section, the orange line at the top represents the theoretical power density after accounting for optical and thermalization losses. The second orange line is the power density corresponding to the total extractable free energy. For the defect density change from 10^{12} to $10^9 \text{ cm}^{-2} \text{ eV}^{-1}$, the surface recombination loss was reduced by $\sim 3.7 \text{ mWcm}^{-2}$. As discussed above, the improvement of surface recombination also enhances the electrochemical energy of electron-hole pairs in the active material. As a result, the device will have a better total power density of extractable free energy. It has changed from 24.4 to 27.2 mWcm^{-2} for interface defect density (D_{it}) change from 10^{12} to $10^9 \text{ cm}^{-2} \text{ eV}^{-1}$. These values correspond to an MPP shift from 505.14 to 645.07 mV. Similarly, the hole transport-related power density loss was reduced from 3.1 to 0.9 mWcm^{-2} . We observe similar trends and very similar values for these bias voltages in the detailed bias-dependent FELA of the solar cell with $D_{it} = 10^9 \text{ cm}^{-2} \text{ eV}^{-1}$, as shown in Figure 6. Note that for $D_{it} = 10^{12} \text{ cm}^{-2} \text{ eV}^{-1}$, a significant amount of free energy power density loss is shifted from hole transport-related loss to surface recombination, even for low bias voltage.

The $\sim 3.7 \text{ mWcm}^{-2}$, reduction in surface recombination for D_{it} change from 10^{12} to $10^9 \text{ cm}^{-2} \text{ eV}^{-1}$, gets redistributed to the

output power density and other recombination loss mechanisms. The output power density improved from 16.8 to 24.6 mWcm^{-2} . The Auger recombination increased from an almost insignificant loss to a loss of around 0.54 mWcm^{-2} . Similarly, the other bulk recombinations also increased, although not to the same extent as Auger recombination. The discussed quantitative changes are illustrated in the line plots in Figure 9b.

For D_{it} of a-Si (i)/c-Si (n) close to zero, the output power density gets to a value around 24.7 mWcm^{-2} . It shows that only a maximum of around 0.2 mWcm^{-2} can be regained for the solar cell discussed in this work, as shown in Figure 6, through improved chemical passivation of the wafer surfaces. Based on the insights gained from the detailed bias-dependent power density losses shown in Figures 6–8, we can regain a considerable power density. It can be regained by improving the hole conductivity (σ_p) at the rear side a-Si:H layers and by decreasing the majority free carrier concentration of the active layer. The latter, lower active dopant concentration on c-Si (n), will limit Auger recombination. These can be seen in Figure 10a,b. Assuming a 30 times larger conductivity value of the rear-side a-Si:H layers compared to the solar cell studied in this work, we calculated a power conversion efficiency enhanced to $\sim 25.4\%$. It aligns with similar trends reported in the literature [5, 35]. Figure 10a depicts the detailed bias-dependent power density losses. The MPP is shifted by around $\sim 15 \text{ mV}$, from ~ 645 to $\sim 660 \text{ mV}$. At the same bias voltage of $\sim 645 \text{ mV}$, the high conductivity of a-Si:H contact layers enables fast carrier extraction, which minimizes the steady-state carrier concentration in the active layer. It implies a reduced quasi-Fermi level splitting (reduced electrochemical energy of electron-hole pairs). Hence, the available power density (P_{eh}) of free energy is reduced, see Figure 10a as compared to Figure 6. The bulk and surface recombination losses also decreased slightly, which is noticeable for Auger and surface recombination. The power density gain from hole transport-related power density loss can be assumed to be shifting the MPP by a certain number of millivolts (mV) toward the V_{OC} . The maximum possible shift in MPP can be calculated as

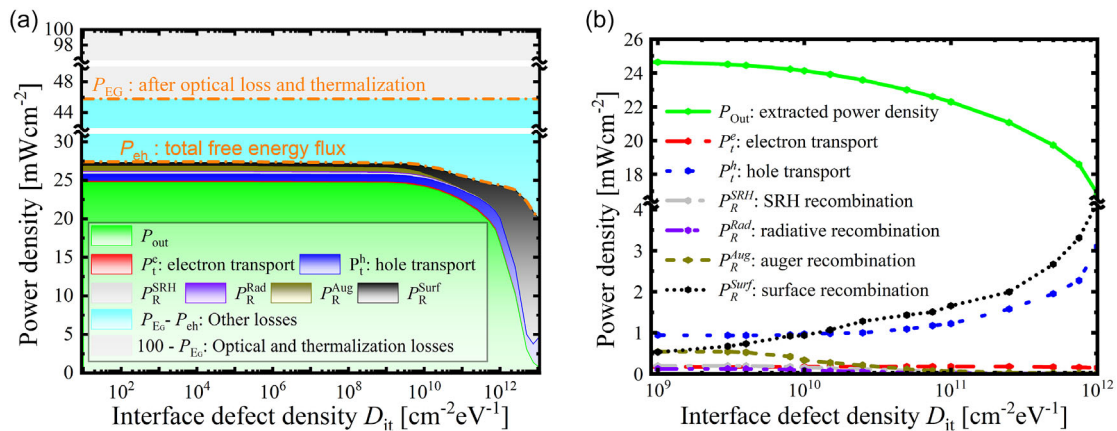


FIGURE 9 | (a) Stacked area plot of detailed power density losses and extracted power density of SHJ solar cells at MPP as a function of a-Si (i)/c-Si (n) interface defect density (D_{it}); (b) line plot showing detailed changes in power density losses for D_{it} change from 10^9 to $10^{12} \text{ cm}^{-2} \text{ eV}^{-1}$. P_t^e and P_t^h stand for power density losses related to electron and hole transport, respectively, including at ITO/Ag contacts. P_R^{Rad} , P_R^{Aug} , P_R^{SRH} & P_R^{Surf} stand for power density loss due to radiative, Auger, SRH, and total surface recombination, respectively. P_{ch} is power density corresponding to the free electrochemical potential energy of the electron-hole pairs. P_{Eg} is power density of theoretically available energy after thermal relaxation and optical losses. The difference between the two orange lines shows other (entropy related) losses.

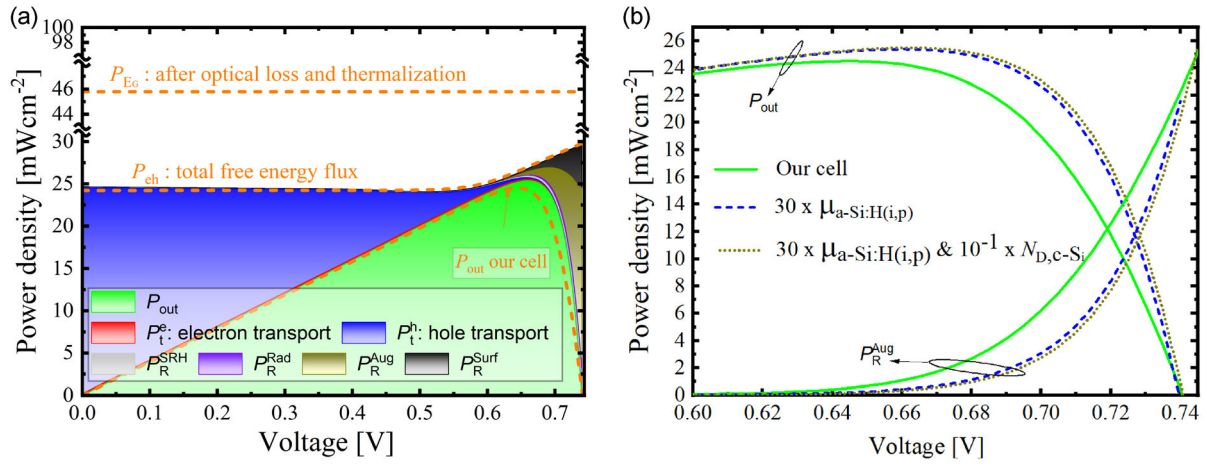


FIGURE 10 (a) Detailed bias-dependent power density losses of an improved solar cell with a thirtyfold enhanced mobility of the a-Si:H layers at the rear side. (b) Comparison of output power density and power density loss due to Auger recombination for an improved a-Si:H layers mobility and active dopant concentration of the c-Si (n). P_{out} stands for output power density of the device. P_t^e and P_t^h stand for power density losses related to electron and hole transport, respectively, including at ITO/Ag contacts. P_{Rad} , P_{Aug} , P_{SRH} , and P_{Surf} stand for power density loss due to radiative, Auger, SRH, and total surface recombination, respectively. P_{ch} is power density corresponding to the free electrochemical potential energy of the electron–hole pairs. P_{Eg} is power density of theoretically available energy after thermal relaxation and optical losses. The difference between the two orange lines shows other (entropy related) losses.

$\Delta V_{MPP} = \frac{\text{Power Density Gain}}{q \cdot J_{ph}}$ by assuming a uniform change in quasi-Fermi level splitting over the volume of the active layer; see Equation (2). J_{ph} represents the photogenerated current density. In Figure 10b, a further improvement of the device can be seen by decreasing the active dopant concentration (N_D) of c-Si (n). An order of magnitude lower active dopant concentration yields a power conversion efficiency of ~25.5%. The improvement primarily stems from the reduction in Auger recombination, as shown in Figure 10b.

The conductivity of semiconductor material is a product of carrier mobility and free carrier density. High-quality a-Si:H with low defect density improves free carrier density. The hole conductivity of a-Si:H layers can be improved by reducing the defect state density, enhancing the doping density, and improving the carrier mobility of the amorphous materials. In Figure 10, the impact of improved conductivity is calculated by enhancing the carrier mobility. A very high active dopant concentration in the a-Si:H (p) can also improve power conversion efficiency by enhancing carrier transport at the HSC, including at the a-Si:H (p)/ITO interface. Note that the thin intrinsic a-Si:H (i) at the wafer interface is essential since a direct deposition of doped a-Si:H on c-Si can lead to degraded a-Si:H/c-Si interface properties [36, 37–38]. Increasing free charge carrier concentration in p-type-doped a-Si:H layer shifts the quasi-Fermi potential of holes in the a-Si:H layers of the HSC layerstack. As a result, the activation energy of a-Si:H (p) and the adjacent intrinsic a-Si:H passivating layer decreases. Hence, it enhances the band bending effect at c-Si (n)/HSC and the hole conductivity of these a-Si:H layers. Furthermore, it modulates the band alignment at the interface a-Si:H (p)/ITO, dictating the band-to-band carrier transport [10, 19].

Figure 11 shows the impact of improvement steps of increasing mobility of a-Si:H silicon, decreasing free majority carrier in c-Si, and increasing active free carrier concentration in doped a-Si:H

layers. The latter also enhances surface recombination through field-effect passivation, as shown in Figure 11a. It results in a ~4 mV increase in V_{OC} and power conversion efficiency of ~25.9%. Figure 11a compares the power density change in the 25.9% efficiency solar cell to our solar cell. The free energy losses are represented by the gap between the blue color for the improved cell and the black color for our cell. Note that the improved solar cell has a lower available free energy in the device for bias voltage below V_{OC} . It shows that with a proper advanced design, one need to improve the available energy while reducing the free energy losses for a high-efficiency solar cell. It involves redesigning a multitude of aspects of the solar cell. Optical improvement is essential to push our cell's J_{SC} beyond 40 mAcm⁻² and power conversion efficiency beyond 26%. The optical losses from reflection and parasitic absorption, shown in Figure 4, are too high and demand optimization. Recent reports indicate that achieving close to 27% efficiency and surpassing it requires minimal shading loss due to metal contact, transparent window layers, and replacing a-Si layers with materials of better properties, such as n-nc-SiO_x:H and nc-Si:H [5, 39]. Lin et al. show that using a highly crystalline nc-Si:H (p), which has four orders of magnitude higher conductivity instead of the conventional a-Si:H (p), enabled the previous record PCE, 26.81%, cell [5]. As stated above, a highly conductive p-type doped layer modulates the conductivity of the adjacent intrinsic thin layer favorably in the HSC of an SHJ solar cell [5, 40].

From the discussion so far, device optimization demands a synergetic improvement of the individual loss mechanisms. The detailed bias-dependent losses presented in this work can be used as a good insight into designing a synergetic performance improvement for solar cells. Note that, however, the FELA equations, Equations (1)–(5), depict the free energy losses due to each corresponding loss mechanism despite these processes being coupled to each other and other mechanisms in the device. Hence, while we can say, with high certainty, how much power

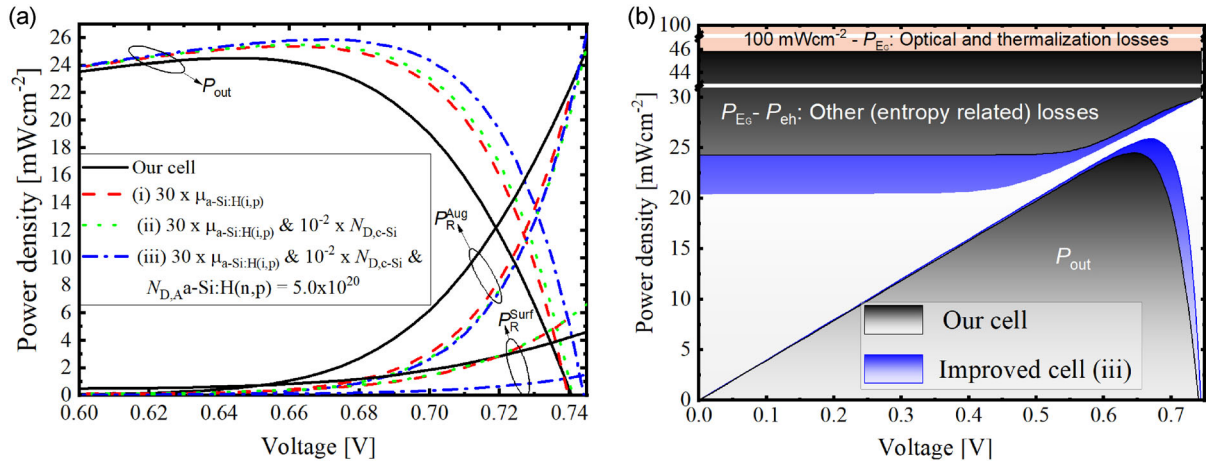


FIGURE 11 | (a) Output power density and dominant recombination losses for device performance improving steps, (b) the incoming power density breakdown for the improved (iii) SHJ solar cell as compared to the SHJ solar cell considered in this work. P_{out} stands for output power density of the device. $P_{\text{R}}^{\text{Aug}}$, and $P_{\text{R}}^{\text{Surf}}$ stand for power density loss due to Auger and total surface recombination, respectively. μ stands for carrier mobility. N_{D} , A a-Si:H (n, p) stands for active dopant concentrations of the doped a-Si:H layers.

density is lost due to each loss mechanism, we cannot know if all the losses can be recovered when each mechanism is improved. To validate how improving each mechanism can enhance the overall performance, one might need to compare the performance before and after the improvement. The so-called Synergistic Efficiency Gain Analysis (SEGA) is based on this idea [41, 42]. The SEGA approach is resource and time-demanding to implement with our electro-optical device model in every situation. The number of needed simulations can be reduced significantly by using a suitable optimization algorithm. We suggest a similar idea coupled with an optimization algorithm, such as a genetic algorithm (GA) [10]. The performance gain will be quantified only for a selected few sets of parameters during each evolution step of the electro-optical device optimization implementation via a GA or other suitable optimization algorithms. It can enable a SHJ-based solar cell redesign with a PCE pushed close to the practical limit of a silicon single-junction solar cell [39, 43, 44].

7 | Conclusion

A device model was developed as a virtual representation of a SHJ solar cell, showing a good agreement with experimental measurements. Our model estimated a prominent optical loss of 3.59 mWcm^{-2} , followed by a parasitic absorption of almost 1.7 mWcm^{-2} in the ITO layers at the front and rear sides. A bias-dependent detailed loss analysis was performed to get insight into the current and power density losses of free energy of photogenerated electron-hole pairs. For this, FELA was implemented on the electro-optical model of the solar cell. The bias-dependent loss analysis showed the breakdown of the free energy for the generated electron-hole pairs in the device at different operating conditions. At lower bias voltages, near short-circuit current conditions, most of the free energy was lost as hole transport related loss in the n-type active layer of c-Si. However, near V_{OC} , the free energy is lost through carrier recombination, mainly via Auger recombination. At MPP, the dominant power density loss $\sim 0.92 \text{ mWcm}^{-2}$ was due to hole transport related

loss. It is primarily at the rear side a-Si:H layer. The remaining losses were approximately 0.67, 0.54, 0.20, 0.12, and 0.11 mWcm^{-2} for surface, Auger, SRH, radiative recombinations, and electron transport related loss, respectively. The detailed bias-dependent free energy loss investigation suggested that the optimization of the front and back contacted monofacial SHJ solar cell considered for this work could be improved significantly by enhancing the conductivity of the rear side passivation layer and lowering the wafer's doping density. Our simulation confirms a power conversion efficiency of close to 26% by pursuing the suggestions. We recommend SEGA coupled with a suitable algorithm-based optimization, such as a GA, to exploit insights that can be gained from bias-dependent detailed loss analysis. This can be a computationally affordable technique to design an efficient device based on tweaking the important details of the device.

Acknowledgments

This work was supported by the (HEMF) Helmholtz Energy Materials Foundry infrastructure funded by the HGF (Helmholtz Association).

Conflicts of Interest

The authors declare no conflicts of interest.

Data Availability Statement

The data that support the findings of this study are available from the corresponding author upon reasonable request.

References

1. C. Gueymard, SMARTS2: A Simple Model of the Atmospheric Radiative Transfer of Sunshine : Algorithms and Performance Assessment (Florida Solar Energy Center, 1995).
2. W. Duan, A. Lambert, K. Bittkau, et al., "A Route towards High-Efficiency Silicon Heterojunction Solar Cells," *Progress in Photovoltaics: Research and Applications* 30, no. 4 (2021): 384–392.

3. P. Würfel and U. Würfel, *Physics of Solar Cells: From Basic Principles to Advanced Concepts* / Peter Würfel and Uli Würfel, 3rd ed. (Wiley-VCH, 2016).
4. K. Yoshikawa, H. Kawasaki, W. Yoshida, et al., "Silicon Heterojunction Solar Cell with Interdigitated Back Contacts for a Photoconversion Efficiency over 26%," *Nature Energy* 2, no. 5 (2017): 1–8.
5. H. Lin, M. Yang, X. Ru, et al., "Silicon Heterojunction Solar Cells with up to 26.81% Efficiency Achieved by Electrically Optimized Nanocrystalline-Silicon Hole Contact Layers," *Nature Energy* 8, no. 8 (2023): 789–799.
6. S. Mariotti, E. Köhnen, F. Scheler, et al., "Interface Engineering for High-Performance, Triple-Halide Perovskite-Silicon Tandem Solar Cells," *Science* 381 (2023): 63–69.
7. E. Aydin, E. Ugur, B. K. Yildirim, et al., "Enhanced Optoelectronic Coupling for Perovskite/Silicon Tandem Solar Cells," *Nature* 623 (2023): 732–738.
8. R. Brendel, S. Dreissigacker, C. Ulzhöfer, N.-P. Harder, and P. P. Altermatt, eds. *Free Energy Losses Analysis for Solar Cells* (NREL Workshop on Crystalline Silicon Solar Cells & Modules, 2008).
9. R. Brendel, S. Dreissigacker, N.-P. Harder, and P. P. Altermatt, "Theory of Analyzing Free Energy Losses in Solar Cells," *Applied Physics Letters* 93, no. 17 (2008): 173503.
10. H. T. Gebrewold, K. Bittkau, K. Qiu, U. Rau, and K. Ding, "Understanding Silicon Heterojunction Solar Cells with nc-SiC/SiO₂ as an Alternate Transparent Passivating Front Contact and Computational Design Optimization," *Solar RRL* 7, no. 7 (2023): 2201051.
11. M. A. Green, "Self-Consistent Optical Parameters of Intrinsic Silicon at 300K including Temperature Coefficients," *Solar Energy Materials and Solar Cells* 92, no. 11 (2008): 1305–1310.
12. E. D. Palik, *Handbook of Optical Constants of Solids* (Academic Press Handbook Series, 1985).
13. Sentaurus Device User Guide (Synopsys Inc., 2015).
14. A. Richter, S. W. Glunz, F. Werner, J. Schmidt, and A. Cuevas, "Improved Quantitative Description of Auger Recombination in Crystalline Silicon," *Physical Review B* 86, no. 16 (2012): 165202.
15. H. T. Nguyen, S. C. Baker-Finch, and D. Macdonald, "Temperature Dependence of the Radiative Recombination Coefficient in Crystalline Silicon from Spectral Photoluminescence," *Applied Physics Letters* 104, no. 11 (2014): 112105.
16. P. P. Altermatt, A. Schenk, F. Geelhaar, and G. Heiser, "Reassessment of the Intrinsic Carrier Density in Crystalline Silicon in View of Bandgap Narrowing," *Journal of Applied Physics* 93, no. 3 (2003): 1598.
17. D. Klaassen, "A Unified Mobility Model for Device Simulation—I. Model Equations and Concentration Dependence," *Solid-State Electronics* 35, no. 7 (1992): 953–959.
18. J. M. Shannon and K. J. B. M. Nieuwesteeg, "Tunneling Effective Mass in Hydrogenated Amorphous Silicon," *Applied Physics Letters* 62, no. 15 (1993): 1815–1817.
19. P. Procel, H. Xu, A. Saez, et al., "The Role of Heterointerfaces and Subgap Energy States on Transport Mechanisms in Silicon Heterojunction Solar Cells," *Progress in Photovoltaics: Research and Applications* 28, no. 9 (2020): 935–945.
20. F. Wang, Y. Gao, Z. Pang, L. Yang, and J. Yang, "Insights into the Role of the Interface Defects Density and the Bandgap of the Back Surface Field for Efficient p-Type Silicon Heterojunction Solar Cells," *RSC Advances* 7, no. 43 (2017): 26776–26782.
21. L. Z. Peng, "Design, Fabrication and Characterization of Thin-Film Materials for Heterojunction Silicon Wafer Solar Cells" (Dissertation, National University of Singapore, 2014).
22. M. Rahmouni, A. Datta, P. Chatterjee, J. Damon-Lacoste, C. Ballif, and P. Roca i Cabarrocas, "Carrier Transport and Sensitivity Issues in Heterojunction with Intrinsic Thin Layer Solar Cells on N-Type Crystalline Silicon: A Computer Simulation Study," *Journal of Applied Physics* 107, no. 5 (2010): 54521.
23. S. Lee, D. P. Pham, Y. Kim, E.-C. Cho, J. Park, and J. Yi, "Influence of the Carrier Selective Front Contact Layer and Defect State of a-Si: H/c-Si Interface on the Rear Emitter Silicon Heterojunction Solar Cells," *Energies* 13, no. 11 (2020): 2948.
24. F.-J. Ma, H. Liu, B. Liao, et al., "Impact of Auger Recombination Parameterisations on Predicting Silicon Wafer Solar Cell Performance," *Journal of Computational Electronics* 13, no. 3 (2014): 647–656.
25. B. A. Veith-Wolf, S. Schäfer, R. Brendel, and J. Schmidt, "Reassessment of Intrinsic Lifetime Limit in n-Type Crystalline Silicon and Implication on Maximum Solar Cell Efficiency," *Solar Energy Materials and Solar Cells* 186 (2018): 194–199.
26. J. Greulich, H. Höfller, U. Würfel, and S. Rein, "Numerical Power Balance and Free Energy Loss Analysis for Solar Cells including Optical, Thermodynamic, and Electrical Aspects," *Journal of Applied Physics* 114 (2013): 20.
27. S. M. Sze and M. K. Lee, *Semiconductor Devices, Physics and Technology*, 3rd ed. (Wiley, 2013).
28. K. R. McIntosh and L. E. Black, "On Effective Surface Recombination Parameters," *Journal of Applied Physics* 116, no. 1 (2014): 14503.
29. N. Brinkmann, G. Micard, Y. Schiele, G. Hahn, and B. Terheiden, "Free Energy Loss Analysis of Heterojunction Solar Cells," *Physica Status Solidi Rapid Research Letters* 7, no. 5 (2013): 322–325.
30. R. Brendel, T. Dullweber, R. Peibst, C. Kranz, A. Merkle, and D. Walter, "Breakdown of the Efficiency Gap to 29% Based on Experimental Input Data and Modeling," *Progress in Photovoltaics: Research and Applications* 24, no. 12 (2016): 1475–1486.
31. G. Micard and G. Hahn, eds., in *Free Energy Loss Analysis Decomposition of the Power Voltage Characteristic of an Interdigitated Back Contact Solar Cell*, 5 pages / 29th European Photovoltaic Solar Energy Conference and Exhibition (WIP, 2014), 1267–1271.
32. A. Polman and H. A. Atwater, "Photonic Design Principles for Ultrahigh-Efficiency Photovoltaics," *Nature Materials* 11, no. 3 (2012): 174–177.
33. Z. R. Abrams, "Thermodynamics, Entropy, Information and the Efficiency of Solar Cells" (Doctor of Philosophy, University of California, 2012).
34. R. T. Ross and T.-L. Hsiao, "Limits on the Yield of Photochemical Solar Energy Conversion," *Journal of Applied Physics* 48, no. 11 (1977): 4783–4785.
35. Z. Wu, W. Duan, A. Lambertz, et al., "Low-Resistivity p-Type a-Si: H/AZO Hole Contact in High-Efficiency Silicon Heterojunction Solar Cells," *Applied Surface Science* 542 (2021): 148749.
36. M. Tanaka, M. Taguchi, T. Matsuyama, et al., "Development of New a-Si/c-Si Heterojunction Solar Cells: ACJ-HIT (Artificially Constructed Junction-Heterojunction with Intrinsic Thin-Layer)," *Japanese Journal of Applied Physics* 31, no. 11R (1992): 3518.
37. D. Pysch, M. Bivour, K. Zimmermann, C. Schetter, M. Hermle, and S. W. Glunz, in *Comprehensive Study of Different PECVD-Deposition Methods for Deposition of Thin Intrinsic Amorphous Silicon for Heterojunction Solar Cells*, 6 pages / 24th European Photovoltaic Solar Energy Conference, Hamburg, Germany, 21–25 September 2009, 1580–1585.
38. M. Schmidt, L. Korte, A. Laades, et al., "Physical Aspects of a-Si: H/c-Si Heterojunction Solar Cells," *Thin Solid Films* 515, no. 19 (2007): 7475–7480.
39. P. Procel-Moya, Y. Zhao, and O. Isabella, "Unlocking the Potential of Carrier-Selective Contacts: Key Insights for Designing c-Si Solar Cells

with Efficiency beyond 28%," *Solar Energy Materials and Solar Cells* 285 (2025): 113504.

40. W. Duan, T. Rudolph, H. T. Gebrewold, et al., "Insights into the Heat-Assisted Intensive Light-Soaking Effect on Silicon Heterojunction Solar Cells," *Solar RRL* 8, no. 19 (2024): 2400383.

41. C. Kranz, J. H. Petermann, T. Dullweber, and R. Brendel, "Simulation-Based Efficiency Gain Analysis of 21.2%-Efficient Screen-Printed PERC Solar Cells," *Energy Procedia* 92 (2016): 109–115.

42. C. N. Kruse, K. Bothe, and R. Brendel, "Comparison of Free Energy Loss Analysis and Synergistic Efficiency Gain Analysis for PERC Solar Cells," *IEEE Journal of Photovoltaics* 8, no. 3 (2018): 683–688.

43. A. Richter, M. Hermle, and S. W. Glunz, "Reassessment of the Limiting Efficiency for Crystalline Silicon Solar Cells," *IEEE Journal of Photovoltaics* 3, no. 4 (2013): 1184–1191.

44. A. Richter, R. Müller, J. Benick, et al., "Design Rules for High-Efficiency Both-Sides-Contacted Silicon Solar Cells with Balanced Charge Carrier Transport and Recombination Losses," *Nature Energy* 6, no. 4 (2021): 429–438.